

Crustal and uppermost mantle structure of SE Tibetan plateau from Rayleigh-wave group-velocity measurements

Yonghua Li · Jiatie Pan · Qingju Wu ·
Zhifeng Ding

Received: 17 February 2014 / Accepted: 27 May 2014 / Published online: 8 July 2014
© The Seismological Society of China, Institute of Geophysics, China Earthquake Administration and Springer-Verlag Berlin Heidelberg 2014

Abstract A shear-wave velocity model of the crust and uppermost mantle beneath the SE Tibetan plateau was derived by inverting Rayleigh-wave group-velocity measurements of periods between 10 and 70 s. Rayleigh-wave group-velocity dispersions along more than 3,000 inter-station paths were measured based on analysis of teleseismic waveform data recorded by temporary seismic stations. These observations were then utilized to construct 2D group-velocity maps in the period range of 10–70 s. The new group-velocity maps have an enhanced resolution compared with previous global and regional group-velocity models in this region because of the denser and more uniform data coverage. The lateral resolution across the region is about 0.5° for the periods used in this study. Local dispersion curves were then inverted for a 3D shear-wave velocity model of the region by applying a linear inversion scheme. Our 3D shear-wave model confirms the presence of low-velocity zones (LVZs) in the crust beneath the northern part of this region. Our imaging shows that the upper-middle crustal LVZ beneath the Tengchong region is isolated from these LVZs beneath the eastern and northern part of this region. The upper–middle crustal LVZ may be regarded as evidence of a magma chamber in the crust beneath the Tengchong Volcanoes. Our model also reveals a slow lithospheric structure beneath Tengchong and a fast shield-like mantle beneath the stable Yangtze block.

Keywords SE Tibetan plateau · Shear-wave velocity · Rayleigh-wave tomography · Group velocity

1 Introduction

It is widely accepted that the on-going collision of the Indian and Eurasian continents led to crustal shortening and thickening in the Himalaya–Tibet region. However, the mechanisms responsible for both the uplift and the crustal thickening remain controversial. The proposed geodynamic models include the continental extrusion model (Tapponnier et al. 1982) and channel flow model (Clark and Royden 2000). The southeastern margin of the Tibetan plateau is located in a tectonic transitional zone between the uplifted Tibetan plateau to the west and the stable Yangtze platform to the east (Fig. 1), and plays a key role in both models. For example, Tapponnier et al. (1982) attribute a significant amount of the continental shortening of the India–Eurasia collision to the southeastward extrusion of the Indochina block along the Red River fault (RRF) during the Oligo-Miocene. However, a number of seismic (e.g. Wang et al. 2003; Li et al. 2008b; Huang et al. 2002, 2012; Yang et al. 2012) and magnetotelluric studies (Bai et al. 2010) presented evidence for low velocity and electrical resistivity in the mid-to-lower crust, which support the crustal flow model, but to date the distribution and geometry of the crustal low-velocity zones (LVZs) observed in this region are still not well constrained.

Surface-wave tomography has proven to be a useful tool in determining lateral velocity variations in the crust and uppermost mantle (e.g. Shapiro and Ritzwoller 2002). A number of surface-wave tomography studies were carried out in the SE Tibetan plateau and its adjacent areas. These surface-wave tomographic studies based on earthquake

Y. Li (✉) · Q. Wu · Z. Ding
Key Laboratory of Seismic Observation and Geophysical
Imaging, China Earthquake Administration, Beijing 100081,
China
e-mail: lyhgeomag@sina.com

Y. Li · J. Pan · Q. Wu · Z. Ding
Institute of Geophysics, China Earthquake Administration,
Beijing 100081, China

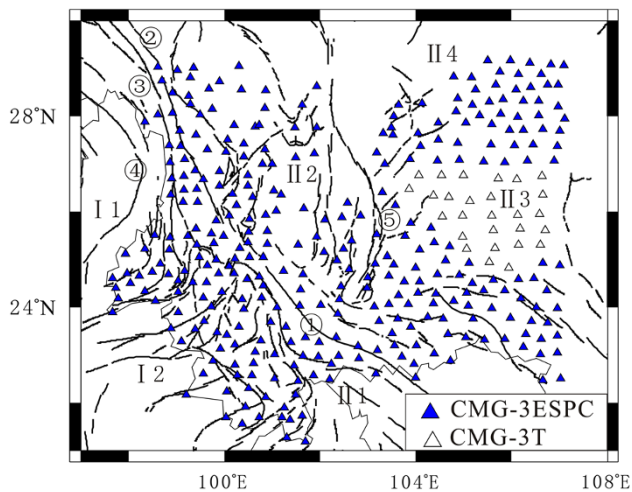


Fig. 1 Map showing the major tectonic units and the locations of stations (*triangles*) used in this study. I Gangwana plate, II Tengchong block, I2 Baoshan block, II South China plate, III Simao block, II2 central Yunnan block, II3 Yangtze platform, II4 Sichuan Basin. ① Red-river fault, ② Jinshajiang fault, ③ Lancangjiang fault, ④ Nujiang fault, ⑤ Xiaojiang fault

data and seismic ambient noise vary from global to local scale (e.g. Shapiro and Ritzwoller 2002; Yao et al. 2008; Hu et al. 2008; Chen et al. 2010; Yang et al. 2010; Li et al. 2013). Larger scale global (e.g. Shapiro and Ritzwoller 2002) and regional surface-wave studies (Li et al. 2013) are sensitive to shear-wave velocity variations in the upper mantle, but lack good constraints on crustal structure and small anomaly bodies. Smaller scale regional and local surface-wave studies (Hu et al. 2008; Chen et al. 2010; Yang et al. 2010) cover the entire study area with relatively high resolution and highlight the existence of notable differences in the crust and upper-mantle shear velocities in different areas, but the detailed shear-wave structure in this region is still under debate.

A high resolution local Rayleigh-wave tomographic study of SE Tibet became feasible when a high-density portable broadband seismic array was set up in December 2008 to image and interpret crustal and mantle structures beneath the southern segment of the north–south seismic belt in China. In this study, seismograms for 92 teleseismic events recorded by 350 broad-band stations were analysed to estimate the interstation Rayleigh-wave group velocity at periods from 10 to 70 s. Then, a tomographic inversion based on traditional ray theory (Ditmar and Yanovskaya 1987; Yanovskaya and Ditmar 1990) was used to construct 2D Rayleigh-wave group velocity maps of SE Tibet using more than 3,000 Rayleigh-wave dispersions with different two-station ray paths. Finally, a 3D shear-velocity model of the crust and uppermost mantle in this region was obtained by inverting the Rayleigh-wave group velocity dispersions.

2 Data selection and group-velocity measurements

The fundamental-mode Rayleigh-wave group-velocity dispersions were measured from vertical-component seismograms recorded by the broadband digital seismograph stations operated by the ChinArray (Phase I). The ChinArray (Phase I) is a temporary network of 325 CMG-3ESPC and 25 CMG-3T broadband sensors deployed in the Yunnan, Guizhou, western Guangxi, and southern Sichuan provinces between September 2011 and April 2013. This array offered a greater station density than had previously been available with the permanent or portable broadband seismological stations in those regions. Figure 1 shows the location of the portable broadband stations used in this study.

All the events that occurred from July 2011 to June 2013 with magnitude (m_b or M_w) greater than 5.5 were initially selected from the USGS NEIC catalogue. In order to obtain good surface-wave energy records, the focal depths were constrained to less than 70 km. Only events with epicentral distances between 10° and 100° were retained to avoid near-source effects and interference from higher-mode Rayleigh waves. The two-station method for surface-wave dispersion analysis is based on the principle that a given earthquake lies along a common great-circle path (GCP) joining the two stations. In accordance with the assumption of the GCP propagation of surface waves, we only used station pairs for which the angle between the back-azimuths of the far station to the epicenter and to the near station was $<4^\circ$. We found 92 events that met the above criteria and were recorded at two stations (Fig. 2).

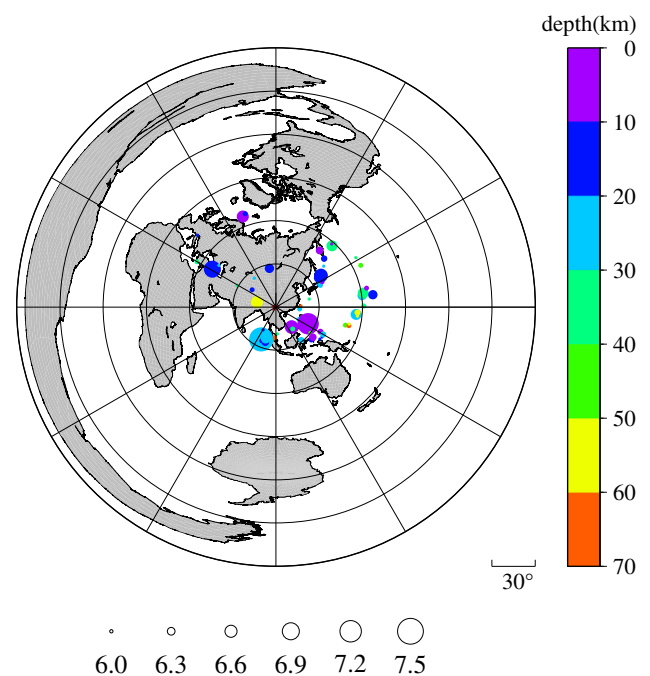


Fig. 2 Azimuthal distribution of events used in this study. Distances between the earthquakes (*solid circles*) and the center of the study area (*star*) ranged from 10° to 100°

To determine the two-station group velocity, we first used Wiener filters to construct the best estimate of the interstation Green’s function, which is the ratio of the smoothed cross-spectrum to the smoothed auto-spectrum of the first station (Hwang and Mitchell 1986). Then the interstation group velocities were measured by applying the CWT frequency time analysis technique (Wu et al. 2009) to these Green’s functions.

The procedures described above were applied to the data of all the selected and processed events, leading to a collection of Rayleigh-wave group velocity dispersions with different period ranges. These dispersions were manually checked for robustness, and then the means for the interstation group dispersions along the individual paths were calculated. Finally, more than 3,000 group velocity dispersions with different paths were constructed. The number of ray paths for the Rayleigh group velocity dispersions at different periods is shown in Fig. 3. The best coverage occurs between 20 and 40 s, and the number of paths decreases at longer and shorter periods. Although the ray paths for the dispersions at the middle periods are slightly denser than those at the shorter and longer periods, the dataset covers a wide range of azimuths across this region, providing a dense sampling of the SE Tibetan plateau (Fig. 4).

3 Rayleigh-wave tomography

3.1 Tomographic method and resolution

The Rayleigh-wave group-velocities were inverted for a set of periods between 10 s and 70 s on a $0.5^\circ \times 0.5^\circ$ grid. The calculations were made by using several smoothing parameters of 0.1, 0.2, and 0.3. A smaller model-smoothing parameter produces a rougher model but a better fit to the data, whereas a larger smoothing parameter will result in a smoother model but worse data fitting. After testing and

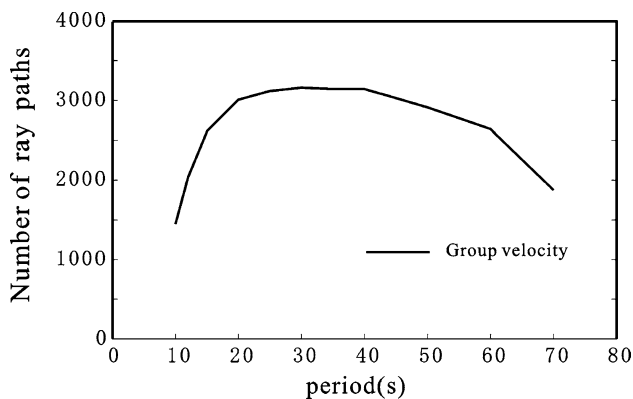


Fig. 3 Number of dispersion measurements as a function of period for Rayleigh-wave group velocities

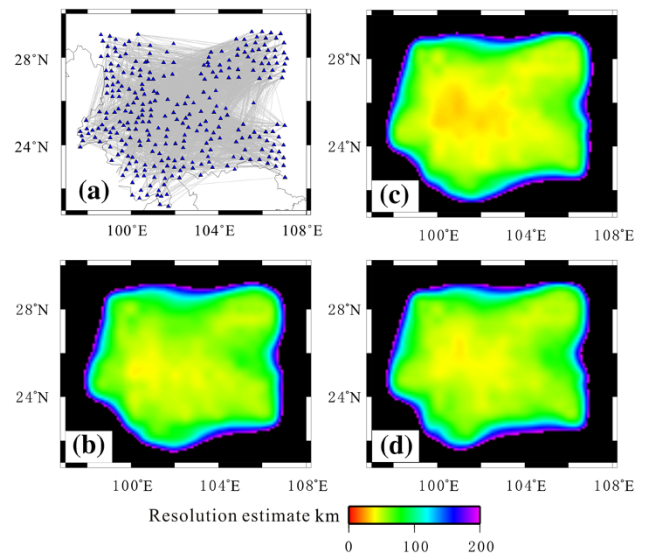


Fig. 4 Data coverage (a) and horizontal resolution maps for Rayleigh-wave group velocity measurements at periods **b** 10 s, **c** 40 s and **d** 70 s

thoroughly inspecting the inversions for various solution errors, model resolution, and model smoothness, we selected 0.2 as the optimal smoothing parameter for our study.

Another criterion used in evaluating the quality of the solution is the comparison of the initial mean square travel-time residual and the remaining unaccounted residual. If for one path the travel-time residual exceeds three times the unaccounted residual, then the corresponding path is eliminated from the data set and the solution is recalculated (Yanovskaya et al. 1998). The number of data points before and after the selection and the initial and remaining mean square travel-time residuals for different periods are listed in Table 1.

During tomography, spatial resolution is also simultaneously evaluated using the method described by

Table 1 Number of measurements and values of the initial and remaining traveltme residual as a function of period for group velocity

Period (s)	Number of initial data	Number of remaining data	Initial residual(s)	Remaining residual(s)
10	1,449	1,375	4.35	2.9
15	2,612	2,453	5.63	2.41
20	3,008	2,891	4.3	2.32
30	3,159	3,091	6.65	2.55
40	3,144	3,056	7	2.45
50	2,911	2,870	5.27	2.74
60	2,638	2,565	4.65	3.01
70	1,877	1,837	4.46	3.17

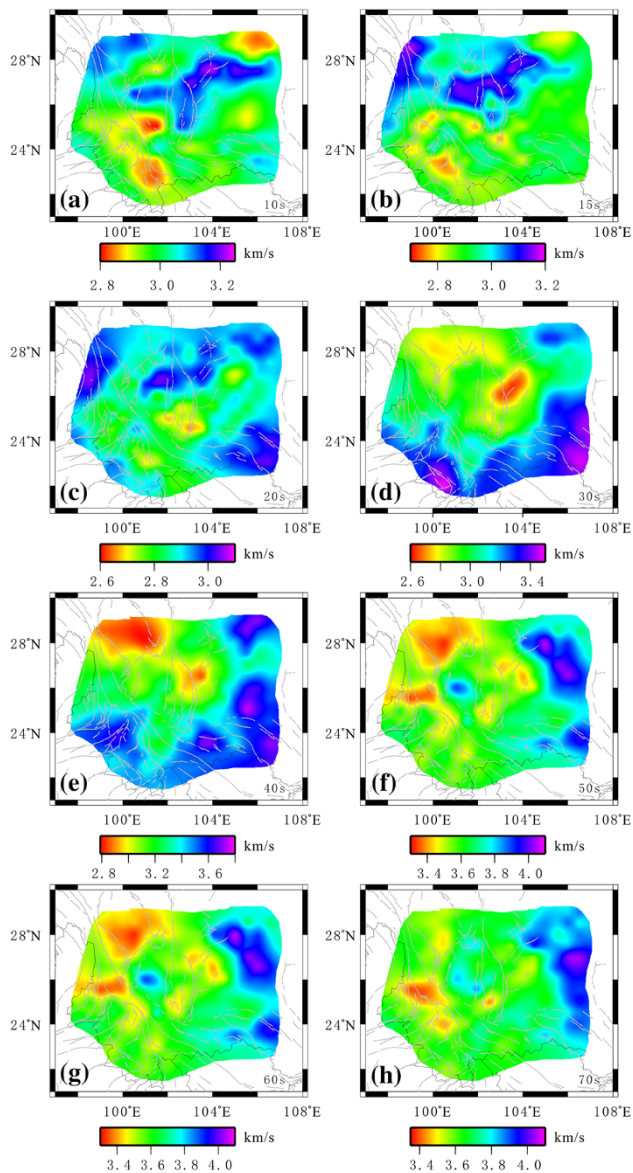


Fig. 5 Fundamental-mode Rayleigh-wave group velocity maps for **a** 10 s period, **b** 15 s period, **c** 20 s period, **d** 30 s period, **e** 40 s period, **f** 50 s period, **g** 60 s period, and **h** 70 s period. Note that a different velocity scale is used for each figure

Yanovskaya (1997), which is similar to that proposed by Backus and Gilbert (1968) for 1D problems. Figure 4 also shows the corresponding resolution for Rayleigh-wave group velocity maps at periods of 10, 40, and 70 s. The average resolution across the SE Tibetan plateau is about 50–100 km for our tomographic maps at 40 s. The average resolution is better than 100 km for the tomographic maps at 10 and 70 s, although it degrades at longer or shorter periods and near the borders of the region where the path coverage is poor (Fig. 4b–d).

3.2 Group velocity maps

We obtained fundamental-mode Rayleigh-wave group velocity maps for eight periods between 10 and 70 s. The Rayleigh-wave group velocity maps at these selected periods are plotted in Fig. 5. These group velocity lateral variations are related to the different tectonic and geological features in this region, as noted by previous surface-wave studies using either earthquake data or ambient noise (e.g. Hu et al. 2008; Chen et al. 2010; Yang et al. 2010; Li et al. 2013). Because of the dense station coverage and ray-paths in the SE Tibetan plateau, our results have substantially better lateral resolution for this region compared to published regional (e.g. Li et al. 2013) and local (e.g. Hu et al. 2008; Chen et al. 2010) group velocity studies. Rayleigh-wave energy penetrates deeper as the wave period increases, and the group velocity at a particular period is related to an integrated average of velocities corresponding to a wavelength-dependent depth.

The Rayleigh-wave group velocity maps at 10 and 20 s (Fig. 5a–c) are primarily sensitive to shear-wave velocity in the upper-middle crust. At periods less than 20 s, the RRF appears to separate the lower-velocity Simao, Baosan and Tengchong blocks from the higher-velocity southwestern Yangtze terrane. This observation suggests a faster Yangtze upper crust compared to the Baosan and Tengchong blocks, confirming and extending into new areas similar observations from active-source refraction/reflection studies (Bai and Wang 2003; Zhang et al. 2005, 2013). The low-velocity anomalies of 0.15–0.20 km/s are observed beneath the Central Yunnan Basin and the southern edge of the Sichuan Basin for periods <20 s, consistent with thick sedimentary layers with thicknesses of up to 10 km (Laske and Masters 1997).

The group velocity maps at periods between 30 and 60 s depict primarily the differences in the crustal thickness and shear velocities in the lower crust and uppermost mantle (Fig. 5d–f). In these maps, the lower group velocities in the northwest and higher velocities in the south and east are preserved. The lower velocities in the northwest that are seen at 30 s period persist to 60 s. This low-velocity zone beneath eastern Tibet corresponds to thicker crust beneath the orogenic belt. The marked positive velocity gradient towards the south and east suggests a gradual decrease in crustal thickness, consistent with observations from receiver function and wide-angle refraction/reflection studies in this region (e.g. Li et al. 2008b, 2014; Zhang et al. 2005, 2011, 2013; Wang et al. 2009; Xu et al. 2013). The extremely low velocities between the RRF and the Xiaojiang fault that are seen at 20 s shift northwards towards the Tibetan plateau at longer periods (30–60 s). This observation along with the low crust–upper mantle velocity and the resistivity anomalies observed in this

region (Li et al. 2008b; Bai et al. 2010; Zhang et al. 2011) imply that the weak lower crust beneath the Tibetan plateau extends into southwest China.

At periods >60 s, the velocity variation evolves from a pattern dominated by the crust to one controlled by lithospheric features. At these longer periods (Fig. 5g, h), large parts of the western Yangtze craton are characterized by a high-velocity anomaly, corresponding to high shear-wave velocities in the Yangtze lithosphere. The existence of high velocity in the uppermost mantle has been imaged in recently published Rayleigh-wave tomography studies (e.g. Li et al. 2013). The western part of the Xiaojiang fault displays overall lower velocities compared to the Yangtze region. The interesting velocity contrasts between the western Yunnan and South China regions suggest that the upper-mantle structure in the South China terrane is distinct from the rest of this region. The most prominent low-velocity anomaly is found beneath the Tengchong volcano region. The low velocities at these longer periods maybe related to high temperatures and/or partially melted material resulting from the subduction of the Burma microplate (Huang and Zhao 2006; Lei et al. 2009) or the Indian plate (Wang and Huang 2004; Hu et al. 2008).

4 Shear-wave velocity structure

4.1 Inversion of local dispersion curves

To obtain an image of the shear-velocity structure of the crust and upper mantle, we inverted for a 1D velocity profile for each $0.5^\circ \times 0.5^\circ$ grid point in the region shown in Fig. 4 using

our Rayleigh-wave group velocities from 10 to 70 s periods. Because the longest period of Rayleigh waves used here is 70 s, we invert only for shear-wave speed down to 150 km depth (which will only be reliable to about 100 km), although we lack resolution at that depth, doing so avoided forcing structure at artificially shallow depths. We use only Rayleigh waves, which are predominantly sensitive to vertically polarized shear-wave speeds (V_{sv}), but for simplicity in this study we also refer to it as the shear-wave speed or V_S model.

A linearized iterative algorithm (Herrmann and Ammon 2004) was performed to obtain our shear-wave velocity model. The earth model was parameterized with layer thicknesses of 1 km at depths of 0–6 km, 2 km at depths of 6–50 km, 5 km at depths of 50–100 km and 10 km at depths of 100–150 km (Fig. 6a). We use the same velocity in the crust and the shallow mantle to avoid forcing a velocity jump at the Moho discontinuity during the inversions. Since Rayleigh-wave dispersion is primarily sensitive to S-wave velocities, only the shear-wave velocity was inverted. The thickness and V_p/V_S in each layer were fixed during the inversion and the density was estimated from the P-wave velocity.

In this study, we used a differential inversion scheme, which minimized both the magnitude of the error vector between the observed and computed velocities and the differences between adjacent layers, to avoid large velocity changes between adjacent layers. When the residual between the observed and predicted dispersions remains constant, the change in models corresponding to the various iterations is negligible.

The inversion of surface waves for seismic velocity structure is a typical non-linear problem. To evaluate the uncertainty of the inversion results, we performed numerous

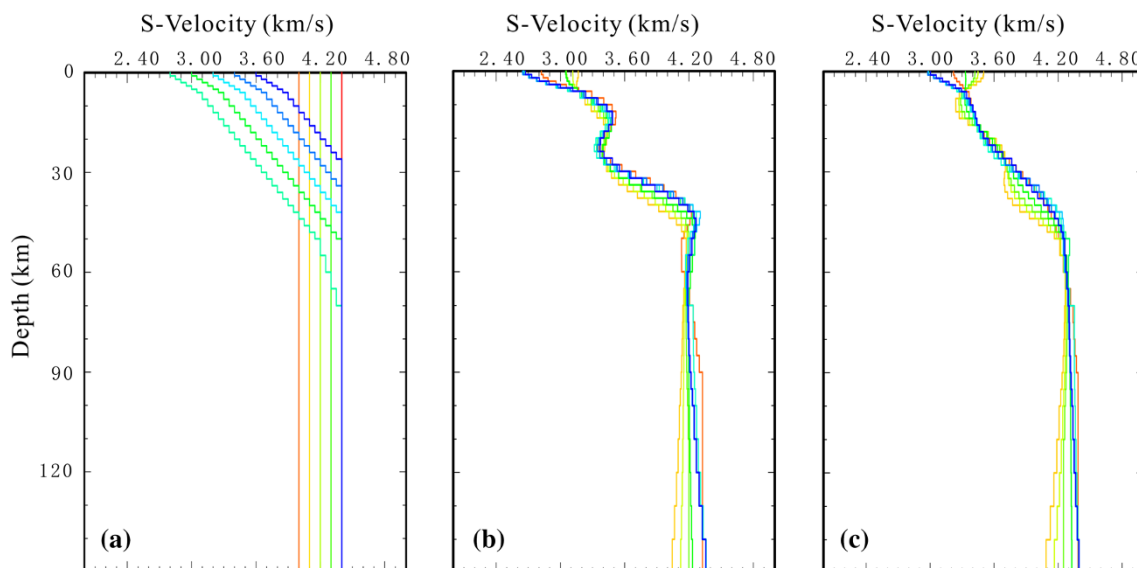


Fig. 6 Inversion results for two different grid points in the SE Tibetan plateau. **a** starting models, **b** and **c** inversion results for grid points (102°E, 23°N) and (105°E, 23°N), respectively. Coloured solid lines in **a–c** indicate the different starting/resulting models

inversions for a range of starting models and analysed the resulting suite of best-fitting models. Our ten starting models bound and evenly spanned the range of velocities seen in Fig. 6. The starting models had one of two velocity gradients (0.01 s^{-1} or constant velocity), and ranged from 2.8–4.4 km/s at the surface and 4.0–4.6 km/s at 150 km depth. The final shear-wave velocity structure was averaged from the 10 inversion solutions. Statistical evaluations showed large uncertainties in the upper crust of our final results. This is not surprising since the dispersion data used for the inversions were larger than 10 s period. Thus, we established that the uncertainty in the inverted models is 0.04–0.2 km/s depending on depth, except in the upper crust.

4.2 Three-dimensional shear-wave structure

Depth slices from the preferred shear-wave velocity model are shown in Fig. 7, and cross sections through the model are shown in Fig. 8. At shallow depths of 10 km, lateral velocity variations partially correlate well with the surface geology. The Central Yunnan Basin and southern edge of the Sichuan Basin are characterized by a lower velocity of about 3.2 km/s, whereas higher velocities of about 3.4 km/s

are found beneath the three-river Orogenic belt to the west and the South China Fold System to the southeast. At 30 km depth, which is in the middle and lower crust, the eastern part and the southwest and northwest regions are characterized by higher velocities of up to 4.0 km/s compared to the remaining areas where the velocities are about 3.1–3.4 km/s. The obvious low-velocity zone (LVZ) in the middle-to-lower crust is seen most clearly in Fig. 6. This is similar to recent surface-wave tomography results of Yang et al. (2012), but we did not observe the LVZs in the eastern and southern part of the study area with normal crustal thickness. At 50 km depth, the wave speeds beneath the northwestern part of the study area are low compared to the surrounding areas, indicating that in the northwestern part the crust reaches down to 50 km depth while in the surrounding area the mantle extends to this depth. In the upper mantle at depths of about 80–120 km (Fig. 7), high velocities are imaged beneath the Yangtze terrane, while low velocities are clearly observed beneath the Tengchong volcano and the adjacent region. The resolution in the Tengchong and western Yangtze is high (Fig. 4); therefore, these velocity anomalies in the upper mantle are not artifacts.

5 Discussion

5.1 The distribution of LVZ and its implications

A prominent feature in our images is the middle-to-lower crustal LVZs beneath the northern part of the Sichuan–Yunnan rhomboidal block (north of $\sim 25^\circ\text{N}$). The distribution of the crustal LVZ is broadly coincident with the area of thick crust, high V_p/V_s ratio (Sun et al. 2012; Xu et al. 2013; Li et al. 2014) and topography in this region. In addition, our LVZs show good spatial correspondence with the high electrical conductivity anomaly observed along two magnetotelluric profiles in this region (Bai et al. 2010). The low velocities (3.1–3.4 km/s), observed beneath the northern part of the Sichuan–Yunnan rhomboidal block at the middle-to-lower crust, are similar to those observed in this area and elsewhere in Tibet (Caldwell et al. 2009; Yang et al. 2012). The LVZs in the mid-lower crust may be related to the presence of partial melts and/or aqueous fluids, which have also been proposed as an explanation for the low-velocity (e.g. Caldwell et al. 2009; Yang et al. 2012), high V_p/V_s ratio (Sun et al. 2012; Xu et al. 2013), and low resistivity magnetotelluric anomalies (e.g. Unsworth et al. 2005; Bai et al. 2010) observed in the Tibetan plateau and its adjacent area. Alternative explanations for the LVZs include the alignment of anisotropic minerals (Yang et al. 2012), which will lead to strong radial anisotropy in the crust. Thus, observations of LVZs in the

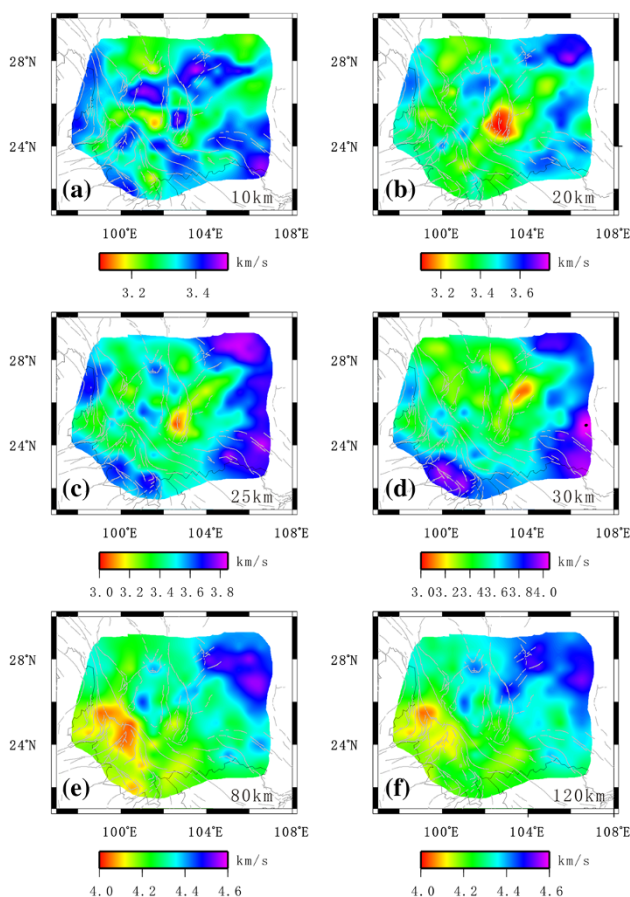


Fig. 7 Horizontal slices of the 3D S-wave velocity model at depths of **a** 10 km, **b** 20 km, **c** 30 km, **d** 50 km, **e** 80 km, and **f** 120 km

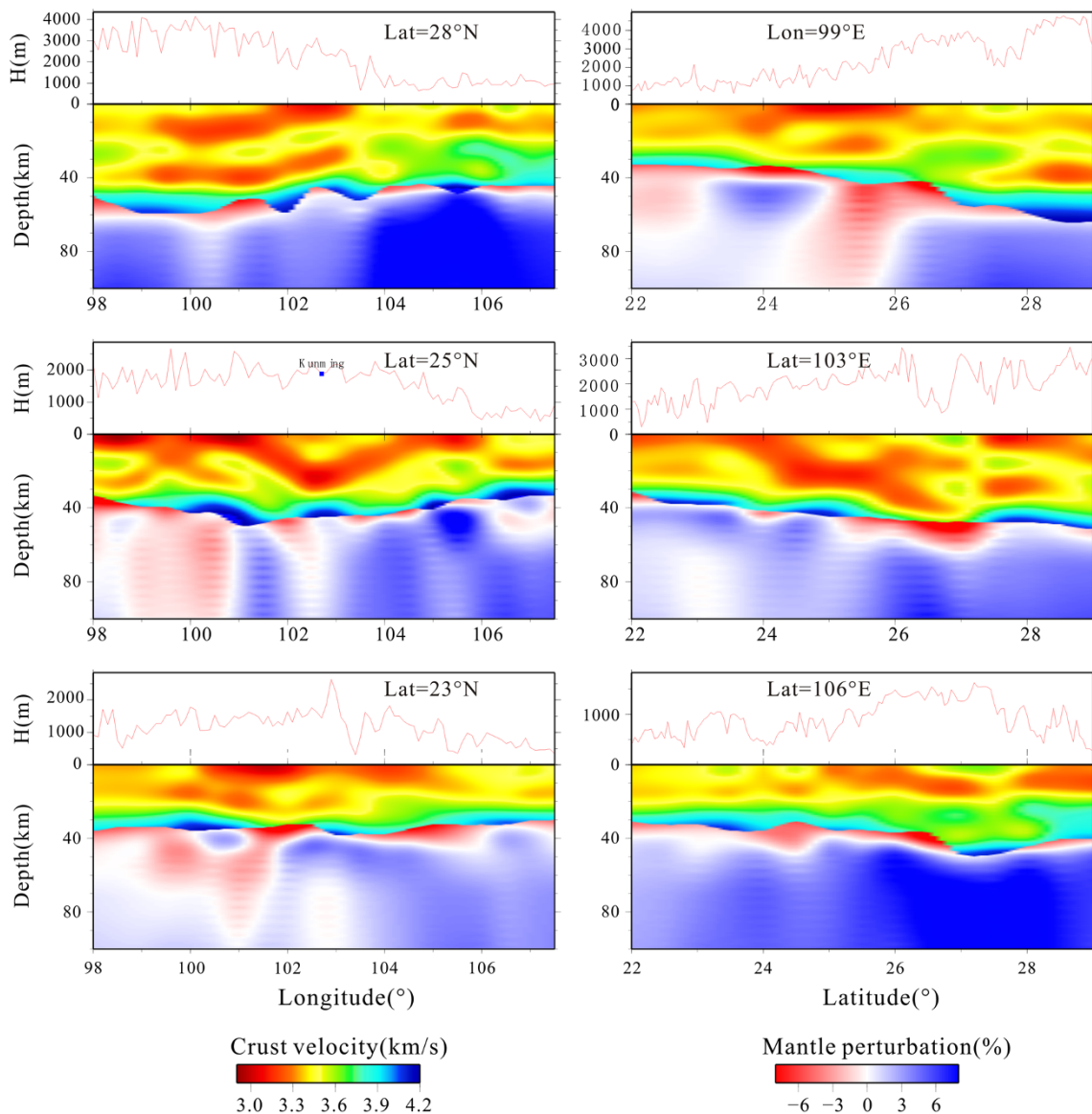


Fig. 8 Vertical slices of the 3D S-wave velocity model plotted along different longitude and latitude lines (shown on panels at top right corner). The reference velocity for the upper mantle is 4.15 km/s. The crustal thickness from Li et al. (2014) is superimposed on the vertical depth profiles. The topography is shown as a red line

middle-to-lower crust imply a weak zone in the crust, although it cannot be used as an argument for the channel flow model.

Our inversion results show that the LVZs are limited to the northern part of the study areas with thickened crust, but the LVZs cannot be observed in the eastern and southern parts of the study areas with normal or slightly thickened crust. In this region, significant changes in lithospheric deformation regime have also been revealed by tele-seismic shear wave splitting studies (Lev et al. 2006; Chang et al. 2006; Wang et al. 2008). Recent surface wave azimuthal anisotropy result furthermore shows that these observed splitting in the eastern and southern parts of

the study areas can be accounted for by upper-mantle anisotropy alone, but for areas on the plateau proper (with thick crust) crustal anisotropy cannot be ignored. These observations are also confirmed by receiver function study (Sun et al. 2012), which revealed significant crustal anisotropy beneath the stations located on the Tibetan plateau and its eastern edge, with averaged splitting time 0.5 s. The N–S transition of shear-wave velocity and anisotropy reflects a fundamental change in the lithospheric structure and deformation regime across this region (Lev et al. 2006; Chang et al. 2006; Wang et al. 2008; Yao et al. 2010). Interestingly, the existence of mechanically weak crust LVZs is needed to explain the crust and mantle

decoupling deformation beneath the northern part of the margin (Yao et al. 2010; Chen et al. 2009). Therefore, all these observations are also consistent with the scenario that the crustal thickening beneath SE Tibet has mainly been built by lower crustal flow (Li et al. 2008b; Sun et al. 2012).

5.2 Slow velocity structure beneath the Tengchong volcanoes

The active Tengchong volcanoes are located in western Yunnan province (Fig. 1). Geological investigations reveal that the Tengchong volcanoes show multi-phase activity from the Miocene to the Quaternary (Jiang 1998). Our images reveal one LVZ in the upper-middle crust beneath the Tengchong volcanoes. At the same time, we also note that the intra-crustal LVZ beneath the Tengchong volcanoes is a small-scale local feature that is isolated from other crustal LVZs. This observation is in good agreement with the recently published crustal S-wave velocity model from joint analysis of receiver functions and Rayleigh-wave dispersion (Sun et al. 2014), but differs from the previous surface-wave tomographic models (Hu et al. 2008; Yao et al. 2008, 2010; Chen et al. 2009; Yang et al. 2012), which only detected one interconnected weak layer instead of two separate zones in this area because of the relatively low resolution of the studies. These intra-crustal LVZs have been interpreted as isolated channels of crustal flow at different depths beneath SE Tibet (Sun et al. 2014). The Tengchong volcanoes are also the area where the middle crust is thought to be sufficiently hot to undergo large-scale horizontal flow (Clark and Royden 2000). In fact, the location of the slow wave propagation also coincides with areas of low upper crust P velocities, resistivity and high heat flow and crustal V_p/V_s (Wu et al. 1988; Sun et al. 1989; Wang and Huangfu 2004; Li et al. 2008b; Lei et al. 2009), which have been used as evidence of a magma chamber in the crust beneath Tengchong. Therefore, another reasonable interpretation of the LVZ in the upper-mid crust beneath this region may be related to the existence of partial melts resulting from upwelling of mantle material.

Our inversion results also show that the slow shear-wave speeds are not confined to the crust, but extend much deeper into the upper mantle, at least in the top 120 km. This is in good agreement with previous tomographic results where the low-velocity anomaly extends down to about 150 km or even to 400 km depth and suggests that Tengchong volcanism is related to the subduction of the Burma microplate (Huang and Zhao 2006; Li et al. 2008a; Lei et al. 2009).

6 Conclusions

In this study, we estimated interstation Rayleigh-wave group-velocity dispersions using teleseismic waveform data recorded by the temporary seismic stations of Chin-Array (Phase I) deployed in SE Tibet. More than 3,000 path-averaged measurements were used to create group-velocity maps at periods of 10–70 s. The resulting dense ray path coverage allowed us to obtain lateral variations of the group velocities with an unprecedented resolution.

We also generated inverted group-velocity maps for local velocity depth profiles using a linear inversion technique. These profiles were then assembled to a 3D model of shear-wave velocity in the crust and uppermost mantle beneath the SE Tibetan plateau. Our new model is not only in good agreement with previous seismic studies in most parts, but also resolves a number of new features. Our 3D shear-wave model shows that LVZs in the crust are confined to the northern part of this region and are not observed across the southern and eastern parts of the region. Our model reveals a distinct zone of low velocities in the upper-middle crust and uppermost mantle beneath Tengchong and implies that Tengchong volcanism is related to the upwelling of hot asthenospheric materials. Fast crustal and mantle velocities were observed beneath the stable Yangtze block.

The detailed model of the crust and uppermost mantle beneath the SE Tibetan plateau provides useful information that improves our understanding of the geodynamic evolution in this region. An on-going study will include Rayleigh-wave phase and receiver function analysis for a joint inversion with these group velocity observations to further constrain the shear-wave velocity structure in this region.

Acknowledgments This study was supported by the China National Special Fund for Earthquake Scientific Research in Public Interest (201008001) and NSFC (41074067).

References

- Backus G, Gilbert F (1968) The resolving power of gross earth data. *Geophys J R Astr Soc* 16:169–205
- Bai ZM, Wang CY (2003) Tomographic investigation of the upper crustal structure and seismotectonic environment in Yunnan Province. *Acta Seismol Sin* 16(2):127–139
- Bai DH, Unsworth MJ, Meju MA, Ma XB, Teng JW, Kong XR, Sun Y, Sun J, Wang LF, Jiang CS, Zhao CP, Xiao PF, Liu M (2010) Crustal deformation of the eastern Tibetan Plateau revealed by magnetotelluric imaging. *Nat Geosci* 3:358–362
- Caldwell WB, Klemperer SL, Rai SS, Lawrence JF (2009) Partial melt in the upper-mantle crust of the northwest Himalaya revealed by Rayleigh wave dispersion. *Tectonophysics* 477:58–65
- Chang LJ, Wang CY, Ding ZF (2006) A study on SKS splitting beneath the Yunnan region. *Chin J Geophys* 49:167–175 (in Chinese with English abstract)

- Chen Y, Badal J, Zhang ZJ (2009) Radial anisotropy in the crust and upper mantle beneath the Qinghai-Tibet Plateau and surrounding regions. *J Asian Earth Sci* 36:302–389
- Chen Y, Badal J, Hu JF (2010) Love and Rayleigh wave tomography of the Qinghai-Tibet plateau and surrounding areas. *Pure Appl Geophys* 167:1171–1203
- Clark MK, Royden LH (2000) Topographic ooze: building the eastern margin of Tibet by lower crustal flow. *Geology* 28:703–706
- Ditmar PG, Yanovskaya TB (1987) A generalization of the Backus-Gilbert method for estimation of lateral variations of surface wave velocity. *Izv Phys Solid Earth* 23:470–477
- Herrmann RB, Ammon CJ (2004) Computer Programs in Seismology. St. Louis. (<http://www.eas.slu.edu/eqc/eqccps.html>). Accessed 28 Nov 2004
- Hu JF, Hu YL, Xia JY, Chen Y, Zhao H, Yang HY (2008) Crust-mantle velocity structure of S wave and dynamic process beneath Burma Arc and its adjacent regions. *Chin J Geophys* 51(1):140–148 (in Chinese with English abstract)
- Huang J, Zhao D (2006) High-resolution mantle tomography of China and surrounding regions. *J Geophys Res* 111:B09305. doi:10.1029/2005JB004066
- Huang J, Zhao D, Zheng S (2002) Lithospheric structure and its relationship to seismic and volcanic activity in southwest China. *J Geophys Res* 107(B10):2255. doi:10.1029/2000JB000137
- Huang J, Liu XJ, Su YJ, Wang BS (2012) Imaging 3-D crustal P-wave velocity structure of western Yunnan with bulletin data. *Earthq Sci* 25:151–160
- Hwang HJ, Mitchell BJ (1986) Interstation surface wave analysis by frequency domain wiener deconvolution and modal isolation. *Bull Seismol Soc Am* 76:847–864
- Jiang CS (1998) Distribution characteristics of Tengchong volcanoes in the Cenozoic Era. *J Seismol Res* 21(4):309–319 (in Chinese with English abstract)
- Laske G, Masters G (1997) A global digital map of sediment thickness. *EOS Trans AGU* 78:F483
- Lei JS, Zhao DP, Su Y (2009) Insight into the origin of the Tengchong intraplate volcano and seismotectonics in southwest China from local and teleseismic data. *J Geophys Res* 114:B05302
- Lev E, Long MD, van der Hilst RD (2006) Seismic anisotropy from shear-wave splitting in Eastern Tibet reveals changes in lithospheric deformation. *Earth Planet Sci Lett* 251:293–304
- Li C, van der Hilst R, Meltzer A, Engdahl E (2008a) Subduction of the Indian lithosphere beneath the Tibetan Plateau and Burma. *Earth Planet Sci Lett* 274:157–168
- Li YH, Wu QJ, Zhang RQ, Tian XB, Zeng RS (2008b) The crust and upper mantle structure beneath Yunnan from joint inversion of receiver functions and Rayleigh wave dispersion data. *Phys Earth Planet Inter* 170:134–146
- Li YH, Wu QJ, Pan JT, Zhang FX, Yu DX (2013) An upper-mantle S-wave velocity model for East Asia from Rayleigh wave tomography. *Earth Planet Sci Lett* 377–378:367–377
- Li YH, Gao MT, Wu QJ (2014) Crustal thickness map of the Chinese mainland from teleseismic receiver functions. *Tectonophysics* 611(25):51–60
- Shapiro NM, Ritzwoller MH (2002) Monte-Carlo inversion for a global shear-velocity model of the crust and upper mantle. *Geophys J Int* 151:88–105
- Sun J, Xu C, Jiang Z (1989) Electricity structure of the crust and upper mantle in western Yunnan and its relation to crust activity. *Seismol Geol* 11(1):35–49 (in Chinese with English abstract)
- Sun Y, Niu FL, Liu HF, Chen YL, Liu JX (2012) Crustal structure and deformation of the SE Tibetan plateau revealed by receiver function data. *Earth Planet Sci Lett* 349–350:186–197
- Sun XX, Bao XW, Xu MJ, Eaton DW, Song XD, Wang LS, Ding ZF, Mi N, Yu DY, Li H (2014) Crustal structure beneath SE Tibet from joint analysis of receiver functions and Rayleigh wave dispersion. *Geophys Res Lett*. doi:10.1002/2014GL059269
- Tapponnier P, Peltzer G, LeDain AY, Armijo R, Cobbold P (1982) Propagating extrusion tectonics in Asia: new insights from simple experiments with plasticine. *Geology* 10:611–616
- Unsworth MJ, Jones AG, Wei W, Marquis G, Gokarn SG, Spratt JE, The INDEPTH-MT Team (2005) Crustal rheology of the Himalaya and Southern Tibet inferred from magnetotelluric data. *Nature* 438:78–81. doi:10.1038/nature04154
- Wang CY, Huangfu G (2004) Crustal structure in Tengchong volcano geothermal area, western Yunnan, China. *Tectonophysics* 380:69–87
- Wang CY, Chan WW, Mooney WD (2003) Three-dimensional velocity structure of crust and uppermantle in southwestern China and its tectonic implications. *J Geophys Res* 108(B9):176–193. doi:10.1029/2002JB0019732442
- Wang CY, Flesch LM, Silver PG, Chang LJ, Chan WW (2008) Evidence for mechanically coupled lithosphere in central Asia and resulting implications. *Geology* 36(5):363–366
- Wang CY, Lou H, Wang XL, Qin JZ, Yang RH, Zhao JM (2009) Crustal structure in Xiaojiang fault zone and its vicinity. *Earthq Sci* 22:347–356
- Wu Q, Zu J, Xie Y (1988) Basical geothermal characteristics in Yunnan Province. *Seismol Geol* 10(4):177–183 (in Chinese with English abstract)
- Wu QJ, Zheng XF, Pan JT, Zhang FX, Zhang GC (2009) Measurement of interstation phase velocity by wavelet transformation. *Earthq Sci* 22:425–429
- Xu XM, Ding ZF, Shi DN, Li XF (2013) Receiver function analysis of crustal structure beneath the eastern Tibetan plateau. *J Asian Earth Sci* 73:121–127
- Yang Y, Zheng Y, Chen J, Zhou SY, Celyan S, Sandvol E, Tilmann F, Priestley K, Hearn TM, Ni JM, Brown LD, Ritzwoller Michael H (2010) Rayleigh wave phase velocity maps of Tibet and the surrounding regions from ambient seismic noise tomography. *Geochem Geophys Geosyst* 11:Q08010. doi:10.1029/2010GC003119
- Yang Y, Ritzwoller MH, Zheng Y, Levshin AL, Xie Z (2012) A synoptic view of the distribution and connectivity of the mid-crustal low velocity zone beneath Tibet. *J Geophys Res* 117:B04303. doi:10.1029/2011JB008810
- Yanovskaya TB (1997) Resolution estimation in the problems of seismic ray tomography. *Izv Phys Solid Earth* 33(9):762–765
- Yanovskaya TB, Ditmar PG (1990) Smoothness criteria in surface wave tomography. *Geophys J Int* 102:63–72
- Yanovskaya TB, Kazima E, Antonova L (1998) Structure of the crust in the Black Sea and adjoining region. *J Seismol* 2:303–316
- Yao HJ, Beghein C, van der Hilst RD (2008) Surface wave array tomography in SE Tibet from ambient seismic noise and two-station analysis-II. Crustal and upper-mantle structure. *Geophys J Int* 173:205–219
- Yao H, van der Hilst RD, Montagner JP (2010) Heterogeneity and anisotropy of the lithosphere of SE Tibet from surface wave array tomography. *J Geophys Res* 115:B12307. doi:10.1029/2009JB007142
- Zhang ZJ, Bai ZM, Wang CY (2005) Crustal structure of Gondwana- and Yangtze-typed blocks: An example by wide-angle seismic profile from Menglian to Malong in western Yunnan. *Sci China* 48(11):1828–1836
- Zhang ZJ, Deng YF, Teng JW, Wang CY, Gao R, Chen Y, Fan WM (2011) An overview of the crustal structure of the Tibetan Plateau after 35 years of deep seismic soundings. *J Asian Earth Sci* 40:977–989
- Zhang EH, Lou H, Jia SX, Li YH (2013) The deep crust structure characteristics beneath western Yunnan. *Chin J Geophys* 56(6):1915–1927 (in Chinese with English abstract)